New insight on spatial localization and microstructures of calcite-aragonite interfaces in adult shell of Haliotis tuberculata: Investigations of wild and farmed abalones by FTIR and Raman mapping

Aïcha Badou, Sylvain Pont, Stéphanie Auzoux-Bordenave, Morgane Lebreton, Jean-François Bardeau

Journal of Structural Biology 214 (2022) 107854

Journal of Structural Biology

New insight on spatial localization and microstructures of calcite-aragonite interfaces in adult shell of *Haliotis tuberculata*: Investigations of wild and farmed abalones by FTIR and Raman mapping

Aïcha Badou [a,*], Sylvain Pont [b], Stéphanie Auzoux-Bordenave [c], Morgane Lebreton [a], Jean-François Bardeau [d]

[a] Direction Générale Déléguée à la Recherche, l'Expertise, la Valorisation et l'Enseignement (DGD REVE), Muséum National d'Histoire Naturelle (MNHN), Station Marine de Concarneau, 29900 Concarneau, France

[b] Institut de Minéralogie, Physique des Matériaux et Cosmochimie (IMPMC), CNRS UMR n°7590, Muséum National d'Histoire Naturelle (MNHN), Sorbonne Université, CNRS, F-75005 Paris, France

[c] Laboratoire de Biologie des Organismes et Ecosystèmes Aquatiques (BOREA), Muséum National d'Histoire Nnaturelle/CNRS/IRD/Sorbonne Université/UCN/UA, Station Marine de Concarneau, 29900 Concarneau, France

[d] Institut des Molécules et Matériaux du Mans (IMMM), UMR CNRS n°6283, Avenue Olivier Messiaen, Le Mans Université, 72085 Le Mans, France

A B S T R A C T

In the present study, we investigated the shell microstructures of the gastropod European abalone *Haliotis tuberculata* in order to clarify the complex spatial distribution of the different mineral phases. Our studies were carried out with a standardized methodology on thirty adult European abalone *H. tuberculata* (5–6 cm long) composed of 15 wild individuals and 15 individuals taken from the France Haliotis hatchery. The macroscopic (binocular) and microscopic observations coupled with Fourier Transform Infrared Spectroscopy (FTIR) and Raman vibrational analysis allowed to unambiguously detect, identify and localize calcite and aragonite. For the first time it has been shown that calcite is present in 100% of farmed and wild adult shell. The microstructural details of the calcite-aragonite interfaces were revealed by using both confocal micro-Raman mapping and Scanning Electron Microscopy (SEM) observations. Calcite zones are systematically found in the spherulitic layer without direct contact with the nacreous layer. The calcite area - nacreous layer interface is made of a thin spherulitic layer with variable thickness from a few micrometers to several millimeters.

In order to contribute to a better understanding of the biomineralization process, a model explaining the hierarchical arrangement of the different phases of calcium carbonate is presented and discussed. Finally, it has been shown that these calcitic zones can be connected to each other within the shells and that their spatial distributions correspond to streaks perpendicular to the direction of length growth.

1. Introduction

Mollusks, like other marine organisms, produce their hard exoskeleton from calcium carbonates (Addadi et al., 2006; Marin et al., 2008; Wilbur and Saleuddin, 1983). From a crystallographic point of view, anhydrous calcium carbonate occurs in three different atomic arrangements or crystalline polymorphs (trigonal calcite, orthorhombic aragonite, and hexagonal vaterite). The formation of calcium carbonate polymorphs from solution has been the subject of research for many years in order to predict and control crystallization phenomena under laboratory conditions for technological applications. Despite intense efforts, the crystallization mechanisms are still not well understood and it appears that the complexity comes from subtle interactions between several factors such as the elementary composition and the presence of organic and inorganic additives, the conditions of initial supersaturation, the temperature, pH and the solvents. Calcite is the more thermodynamically stable of the three polymorphs at ambient conditions (temperature and pressure) and the other two anhydrous crystalline forms are metastable, with vaterite being the least stable polymorph (de Leeuw and Parker, 1998).

The main polymorphs of calcium carbonate found in mollusk shells are predominantly aragonite then calcite (Farmer, 1974; Schrader et al.,

* Corresponding author at: Station Marine de Concarneau-MNHN, Place de la Croix, 29 900 Concarneau, France.
E-mail address: aicha.badou@mnhn.fr (A. Badou).

https://doi.org/10.1016/j.jsb.2022.107854

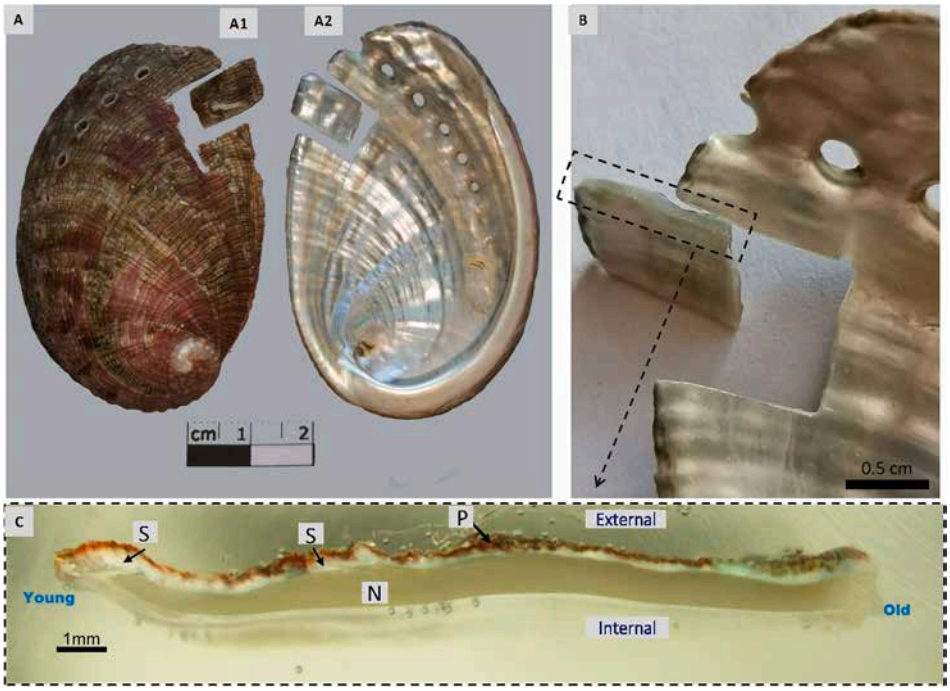

Fig. 1. Abalone shell and location of the cross-section for the study of 15 wild abalone and 15 individuals from the "France Haliotis" hatchery. (A): Adult shell of Haliotis tuberculata (A1) external face (periostracum) (A2) and nacreous internal face. (B) Orientation of the studied section. (C) Binocular view of a sample in cross-section showing the periostracum (P), the nacreous inner layer (N) and the spherulitic outer layer (S).

2000) and in a more limited number of cases vaterite (Frenzel and Harper, 2011; Spann et al., 2010). Investigating the biomineralization mechanisms of calcium carbonate are of considerable interest in particular to better understand how the growth and living environment influence the biomineral organization. Mollusk shell is initiated during early stages of larval development (trochophore stage) and develops through the entire life cycle from larval to post larval and juveniles (Auzoux-Bordenave et al., 2010; Auzoux-Bordenave et al., 2015; Courtois de Viçose et al., 2007; Hickman, 2001; Iwata, 1980; Jardillier et al., 2008; Gaume et al., 2011) to produce the highly organized adult shell.

The mollusk shell is a composite biomaterial formed of a mineral phase ($CaCO_3$ about 95 wt%) and organic matrix (about weight 5%) secreted by the mantle epithelium (Jolly et al., 2004, Schneider et al., 2012; Watabe, 1988). The organic matrix is a mixture of proteins, glycoproteins, lipids, chitin and acidic polysaccharides driving crystal nucleation, selecting the $CaCO_3$ polymorph and controlling the growth and spatial arrangement of minerals (Falini et al., 1996; Levi-Kalisman et al., 2001; Pokroy et al., 2007).

Numerous researches have been carried out on the inner nacreous layer of several mollusks. The number of publications has increased since the year 2000 with the development of research on biomaterials and in the case of the abalone *Haliotis* many research groups have been focused in characterizing the structural properties of the inner layer (Ajili et al., 2020; Blank et al., 2003; Copper et al., 2009; Cusack et al., 2013; Gilbert et al., 2008; Gries et al., 2009; Heinemann et al., 2011; Jackson et al., 2010; Lin and Meyers, 2005; Lopez et al., 2011; Rousseau et al., 2005; Yao et al., 2008).

The shell of *Haliotis tuberculata* is composed of three superimposed layers: the organic periostracum, the outer spherulitic layer and the inner nacreous layer. While the nacreous layer is exclusively composed of aragonite, the outer shell layer may contain both aragonite and calcite (Bøggild 1930; Dauphin et al., 1989; Jolivet et al., 2015; Jolly et al., 2004; Mutvei et al., 1985).

Bøggild (1930) who mentioned two aragonitic layers with the presence of small calcitic spots initiated the first studies of the outer layer in *H. tuberculata* adult. Sabatier (1953) and Bouillon (1958) confirmed then that the external layer is composed of calcite and aragonite. Kessel (1935) using a Feigl's stain method, remarked that in *H. tuberculata* shell, aragonite and calcite are not separated into distinct layers and that numerous aragonitic granules are imbricated into calcitic prisms. These observations were later confirmed by Dauphin et al. (1989) while Brown (1975) indicated a calcitic outer layer and aragonitic inner layer.

After all these controversial observations, Mutvei et al. (1985) studied 8 species of the genus Haliotis including *H. tuberculata*. Mineralogical studies were performed both by decalcification and Feigl's stain and SEM observations on thin and ultrathin slides. The authors described the microstructural organization of the outer layers and specified the presence of calcite (in the form of small points) in the outer shell of *H. tuberculata*. It should be noted that the investigations were carried out on a limited number of samples (one shell per specie) of unknown origin from collections. Consequently, their conclusion needs to be carefully considered and should be extended with a larger number of samples. Nevertheless, this latter article summarized perfectly the scientific motivations related to the presence of calcite in adult shells and suggested different interpretations of shell mineralogy in *H. tuberculata*. More recently, Dauphin et al. (2014) used FTIR and SEM and reported on the spatial and chemical relationship between aragonite and calcite at a microscale. The authors, who underlined the structural complexity and the difficulties of analyzing samples with irregular structures, reported also unexpected results with the coexistence of aragonite plates embedded in a calcite matrix. The contrasting results between the above-mentioned studies were likely due either to individual variations within the abalone (age, season, genetic origin) and/or to differences in spatial resolution. In the case of *H. tuberculata* a single shell was generally studied.

To better understand the spatial distribution of the different mineral phases, the present study investigated the shell mineralogy and microstructure of adult abalone *H. tuberculata* by using a combination of SEM, FTIR and Raman spectroscopies and Energy-dispersive X-ray spectroscopy (EDS/EDX) analysis. A large set of individuals ($n = 30$) of known origin collected from both wild and farmed sites (15 specimens/site) were analyzed and compared according to a standardized methodology.

Our investigations focused on mineral layers and more particularly the outer layer in order to study the micro-structures of calcite-aragonite interfaces. Fourier Transform Infrared Spectroscopy (FTIR) and Raman spectroscopy are powerful, nondestructive and well-known methods for identifying the crystal structure of materials and for studying polymorphs of carbonates in particular (Amarie et al., 2012; Beuvier et al., 2013; Kaczorowska et al., 2003; Schrader et al., 2000; Zakaria et al., 2008). The selection rules of the infrared and Raman spectroscopies make these techniques complementary, and together they can be used to detect and reveal the presence of different $CaCO_3$ polymorphs (Beuvier et al., 2013; Dandeu et al., 2006; Trinkler et al., 2011). In addition, due to the high spatial resolution of the confocal Raman micro-spectroscopy, Raman mapping can be employed to reveal the spatial distribution of polymorphs at the micrometric scale. These investigations will be completed by Scanning Electron Microscope (SEM) and Energy-dispersive X-ray spectroscopy (EDS/EDX) analysis to visualize the distributions of the chemical elements. The detection limits of EDS depend on several factors such as the atomic elements and, the chemical composition of the analyzed sample, the surface roughness, and the characteristics of the spectrometer and the parameters of the electron beam. It is commonly admitted that EDS has a detection limit around 1000 ppm but some authors reported detections limits up to 500 ppm or 100 ppm comparable to those reached by the wavelength dispersive spectrometry for flat, polished and chemically homogenous samples (Lifshin and Gauvin, 2003; Newbury et al., 2017). According to this, EDS X-ray mapping seemed perfectly suited to the detection of trace elements in flat and polished samples homogenously composed of $CaCO_3$. Furthermore, EDS allows a fast simultaneous acquisition on an energy range of a complete X-ray emission spectrum per pixel and accommodates the environmental conditions necessary to the study of our non-carbon-coated samples of abalone shells.

Accordingly, the combination of optical, chemical and structural investigations of wild and farmed adults *H. tuberculata* allowed us to understand the hierarchical arrangement of the different phases of calcium carbonate within the spherulitic layer and the nacreous layer. Different hypotheses will be proposed and discussed to explain their appearance. A schematic reconstruction of different layers and microstructures in relative chronology throughout the growth ages will be proposed to finally explain the reasons of the controversial observations for decades. Finally, through the analysis of puzzle sections of shells, we will show that the calcite zones are not distributed randomly but form streaks perpendicular to the shell growth direction.

2. Materials and methods

2.1. Adult shell samples: Haliotis tuberculata

Adult abalone *H. tuberculata*, 5 to 6 cm in length (Fig. 1A), were collected in April 2015: 15 individuals originated from the France Haliotis abalone farm (Plouguerneau, Brittany, France) and 15 wild individuals were collected in their natural habitat (Moëlan-sur-mer, Brittany, France) by scuba diving at about 8 m depth with the authorization of the Interregional North Atlantic Direction. As reproduction cycle is well controlled in France Haliotis, their adult abalones can be compared to wild specimen on which we have less information on age.

After dissection of the soft tissues, the shells were rinsed with distilled water, dried and stored at room temperature until analysis.

2.2. Sample preparation

The shells were cut with diamond discs, respecting the same localization (Fig. 1A-B), and embedded in Epoxy 2020 resin. The faces were then polished (Fig. 1C) by using different diamond silicon carbide and grain size papers (down to 1 μm). Visual checks were systematically carried out using a binocular during polishing. In order to eliminate the hypothesis of a possible mineral transformation by polishing, Raman and FTIR characterizations were first performed on fractures and then on polished sections.

2.3. FTIR and Raman analysis

2.3.1. FTIR analysis and mapping

The mineralogical composition of the abalone shell sections was analyzed using FTIR spectroscopy in reflectance mode at room temperature (22 °C). Moreover, Attenuated Total Reflection Fourier Transform Infrared (ATR-FTIR) mapping were performed using a germanium crystal (objective 20x) attached to a Bruker Hyperion, 2000 confocal microscope (Bruker Optics, Ettlingen, Germany) equipped with a liquid nitrogen cooled MCT-D316-025 (mercury-cadmium telluride) detector. IR spectra were recorded from 4000 cm^{-1} to 650 cm^{-1}, with a spatial resolution of 20 μm and a spectral resolution of 4 cm^{-1} with 64 scans by pixel. The spectra are shown in absorbance without baseline correction.

Acquisition and spectral analysis were performed using the OPUS Software version 7.0 (Bruker Optics, Ettlingen, Germany).

The chemical composition and spatial location were determined by means of a multivariate approach. Multivariate analysis was performed to extract the maximum useful information about $CaCO_3$ polymorphs embodied in the spectral dataset. Principal component analysis (PCA) was used, without pre-processing treatment, in the wavenumber range 900–690 cm^{-1} to reveal spectral features.

A score plot gives information about the multidimensional structures, and in our case the representation of the score values of the first component, with a chromatic scale going from blue (minimum) to red (maximum score value), recreate in a 2D false color map, the spatial distribution of the aragonite and calcite areas.

2.3.2. Confocal Raman analysis and Raman mapping

The Raman measurements were performed at room temperature using a WITec Alpha 300R confocal Raman spectrometer (WITec GmbH, Ulm Germany) equipped with both a RayShield Coupler and a 1800 gmm^{-1} grating blazed at 500 nm allowing spectra measurements at extremely low wavenumbers and high spectral resolution and a thermically Peltier-cooled Si-based CCD front-illuminated detector (Andor, Oxford Instrument, Belfast, Ireland). Calibration of the spectrometer was achieved by recording the Raman spectrum of an internal Mercury-Argon lamp. Raman scattered signals were collected under a microscope equipped with a Zeiss EC Epiplan-Neofluar® 50xobjective (numerical aperture of 0.55) and a 20x objective (numerical aperture of 0.5) focusing the 532 nm line of a Solid State Sapphire laser (Coherent INC., Santa Clara, USA) on the samples. After having verified that no particular degradation of the samples and spectral modification were observed with a laser power of 40 mW on the sample and integration times of several minutes, we decided to keep fixed this laser power condition and modulate the integration time according to the specific investigations.

The single Raman spectra were systematically recorded 10 times in the wavenumber 25–1200 cm^{-1} region (spectral resolution of 0.7 cm^{-1}) with an integration time of 5 s and averaged to improve the signal-to-noise ratio. The spectrometer being equipped with a motorized scanning stage, large mapping areas were also performed. 52 500 spectra were first recorded from a large mapping 1360 × 538 μm^2 area (2D map step size of around 3.6 μm) with the 50x objective (Fig. 5) and then 38 500 spectra (2D map step size of 2 μm) from a specific area of 1100 × 140 μm^2 with a 50x objective (numerical aperture of 0.55) in order to investigate the calcite-aragonite interfaces with higher spatial resolution. In both cases, the integration times were set at 0.3 s.

The spectral analysis was performed using the WITec Project FIVE plus software (version 5.248, WITec GmbH, Germany) and in particular the True Component Analysis (TCA). This dedicated tool of the WITec Project FIVE plus software allows both identifying pixels of a map with similar spectral features and providing these spectral characteristics (i.e. similar chemical response) in an intensity distribution image. Let us note

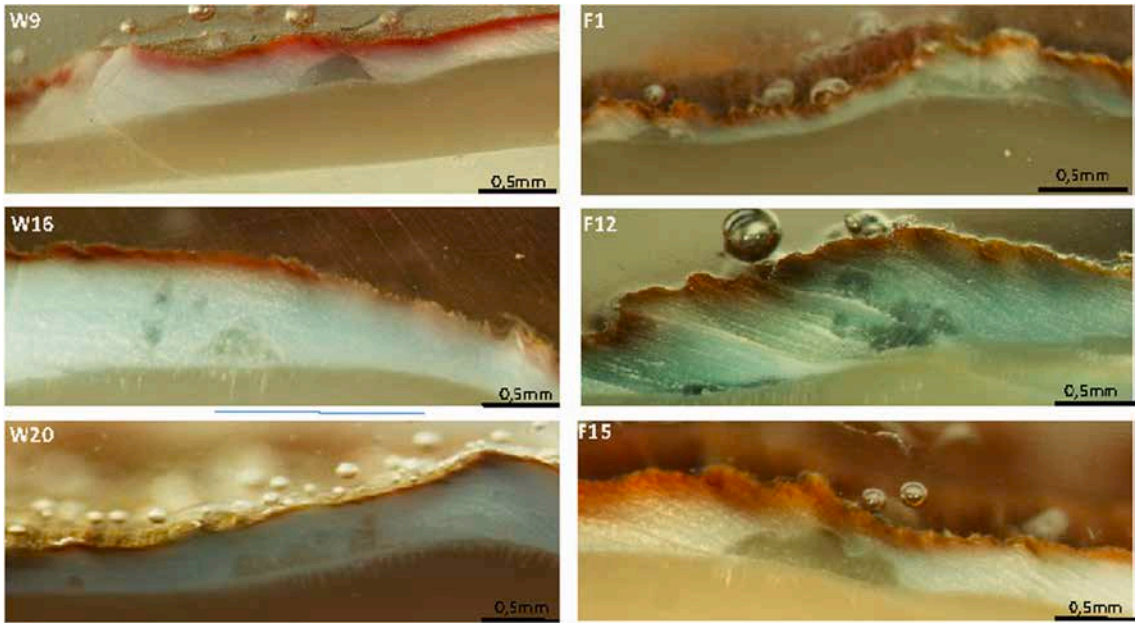

Fig. 2. Images recorded under binocular microscope: some examples of the diversity of areas in the cut-cross of the Wild (**W**) and in the Farm (**F**) shells of *H. tuberculate*, in the left and in the right respectively.

that before analysis, spectral raw data were baseline corrected and preprocessed by removing the cosmic rays.

2.4. Scanning electron microscopy and EDS mapping

2.4.1. Scanning electron microscopy (SEM)

The surface of the samples was observed and analysed using a Zeiss SIGMA300 field emission gun scanning electron microscope (FEG-SEM). High resolution SEM images were obtained by collecting secondary electrons (SE) using an Everhart-Thornley detector with an acceleration voltage of 15 kV. Prior to observations, the samples were mechanically broken and the shell sections were fixed directly on the SEM stubs and then coated with a gold layer of about 10 nm thick.

2.4.2. X-ray mapping

In order to chemically discriminate calcite from aragonite, we acquired X-ray maps of Mg and Na on an uncoated polished thick section of an abalone shell embedded in an epoxy resin. Since we needed to avoid carbon coating of the sample surface for further analyses, the measurements were performed under environmental conditions using a residual nitrogen pressure of 14 Pa inside the SEM analysis chamber. X-ray mapping was recorded with a VEGAII LSU (TESCAN, Czech Republic) scanning electron microscope equipped with an energy dispersive X-ray spectrometer (SEM-EDS). The electron beam was accelerated under a voltage of 15 kV and a virtual diaphragm was selected so that the diameter of the spot was about 430 nm on the sample surface. The BRUKER X-Flash silicon drift detector (Bruker Nano GmbH, Berlin, Germany) was set with the smallest time constant corresponding to a

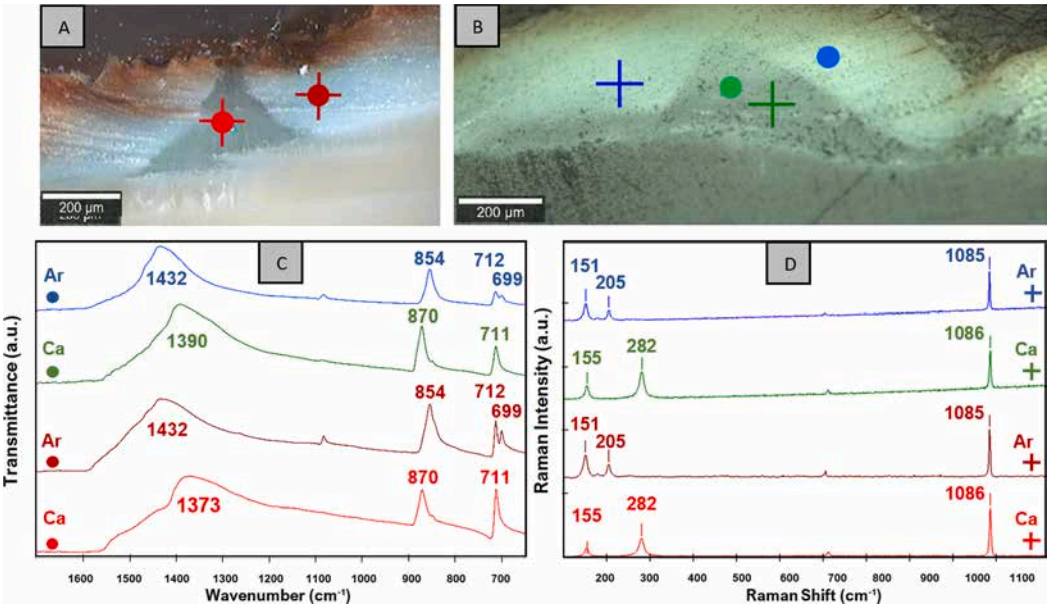

Fig. 3. Images of two sections of wild (A) and farmed (B) abalone *H. tuberculata*. The positions of the points analyzed by FTIR (discs) and Raman (crosses) are marked on the images. FTIR spectra (C) and Raman spectra (D) show two different mineral phases: aragonite (Ar) and calcite (Ca).

Table 1
Peak positions of Raman and infrared bands of calcite and aragonite.

Aragonite		Calcite		
Infrared $\bar{\nu}(cm^{-1})$	Raman $\bar{\nu}(cm^{-1})$	Infrared $\bar{\nu}(cm^{-1})$	Raman $\bar{\nu}(cm^{-1})$	Assignment
–	152	–	155	T
–	205	–		T
–	–	–	282	T
699	701	711	712	
712	705			$\bar{\nu}_4$
854	–	870	–	$\bar{\nu}_2$
1082*	1085	–	1086	$\bar{\nu}_1$
1432	NR	1373–1390	NR	$\bar{\nu}_3$

$\bar{\nu}_1$: Symmetric CO_3 stretching mode; $\bar{\nu}_2$: Asymmetric CO_3 deformation; $\bar{\nu}_3$: Asymmetric CO_3 stretching mode; $\bar{\nu}_4$: Symmetric CO_3 deformation. T: Translational Lattice Mode (Ca, CO_3); NR: not recorded (Frech et al., 1980, White, 1974).

throughput of 275 000 counts per second. The detector collected then for each pixel (HyperMap mode) the relative abundance of emitted X-rays versus their energy in the range 1–10 keV with a resolution of 133 eV. High-resolution chemical images (1024 × 1024 pixels) of the area of interest were compiled during a live counting time of 9 h. The pixel size and the scan speed were respectively of 1.4 μm, and 16 μs/pixel. We chose the step size of the X-ray map according to a Monte-Carlo simulation of the X-ray depth emission profile in a thick homogenous layer composed of $CaCO_3$ (Drouin et al., 2007 ©Casino Version 2.42). The Ca Kα lines are the deepest detected radiations due to their relative high energy in comparison with the ones of Mg or Na. The maximum detection intensity is located at 900 nm under the surface so we selected a pixel size of 1.4 μm in order to detect approximatively 80% of the calcium X-rays and to avoid over sampling which would have lower the accuracy of the mapping.

3. Results and discussions

The binocular observations clearly show that the shell of *H. tuberculata* consists of three major layers (Fig. 1C): the organic periostracum (P); an outer spherulitic aragonite layer (S) and the inner nacreous layer (N). In the spherulitic layer, millimeter size tinted areas with different irregular shapes can be observed (Fig. 2). These latter can be seen on all shells regardless of their origin, i.e. for both wild (W) and Farm (F) shells. Then, two samples from each origin (W and F) have been selected and examined by vibrational spectroscopies (FTIR and Raman) and chemical element analysis (EDS) in order to ensure correct identification of the biominerals and their crystalline structure. Finally, the shell sections were imaged with SEM to identify the microstructures of the different layers as well as their respective location in relation to these tinted areas.

3.1. Identification of $CaCO_3$ polymorphs using FTIR and Raman spectroscopy

The carbonate minerals have been the subject of a large number of studies, theoretically by using a quantum mechanical approach (de la Pierre et al., 2014) and experimentally by using a variety of techniques (Carteret et al., 2013; Couture, 1947; Frech et al., 1980; Urmos et al., 1991; Valenzano et al., 2006). The selection rules of the infrared and Raman spectroscopies make these techniques complementary, and together they can be used to detect and reveal the presence of different $CaCO_3$ polymorphs (Dandeu et al., 2006; Trinkler et al., 2011; Beuvier et al., 2013).

Macroscopic and microscopic observations (Fig. 3 A and B) of wild and farm specimens can reveal optical contrasts in the macrostructure of shell sections. FTIR (Fig. 3C) and Raman (Fig. 3D) investigations both

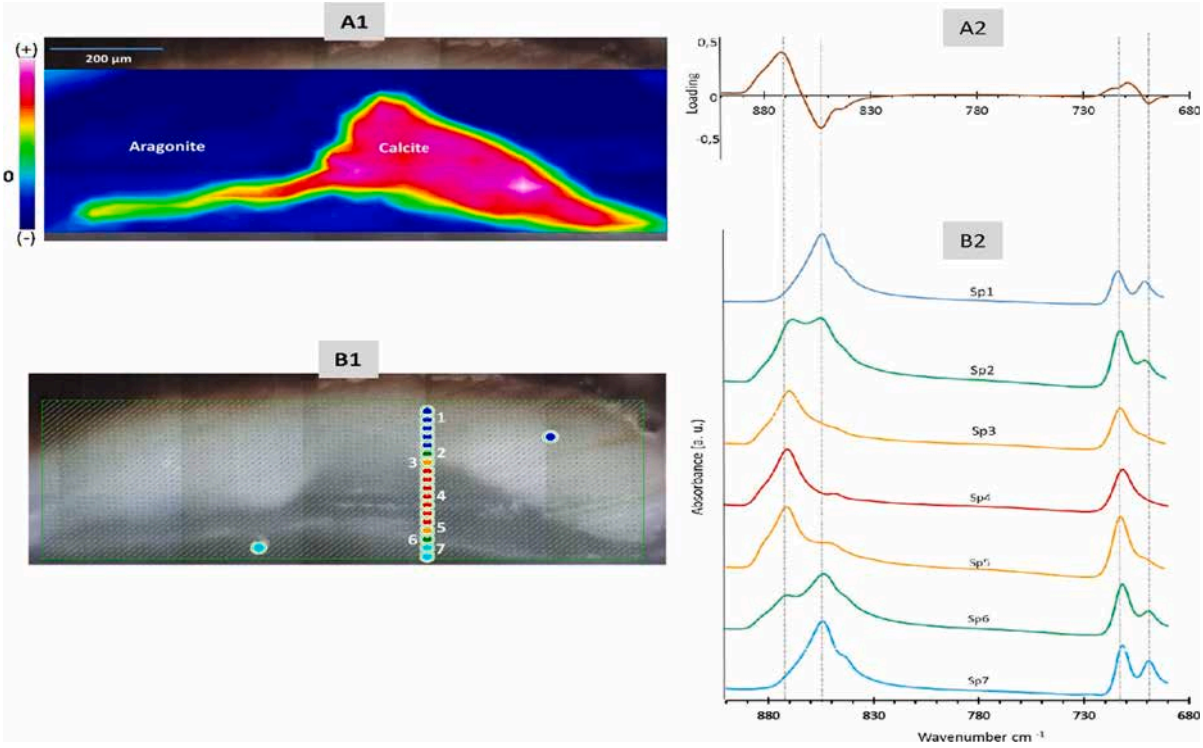

Fig. 4. FTIR mineralogical mapping of a cross-section shell of *H. tuberculata*. (A1): Score corresponding to the representation of the factor bands resulting from the PCA statistical analysis in the range 900–690 cm^{-1}. PC1 represents 34% of the total variance. The score representation of the PC1 shows a calcite-rich central zone and an aragonite-rich peripheral zone. (A2) Loading vectors for PC1 indicating peaks contributing to the PC1 score. (B1) Transect and localisation of the recorded spectra presented in B2. (B2) Corresponding spectra. The notation Sp1 to Sp7 corresponds to the localisation on the transect in B1.

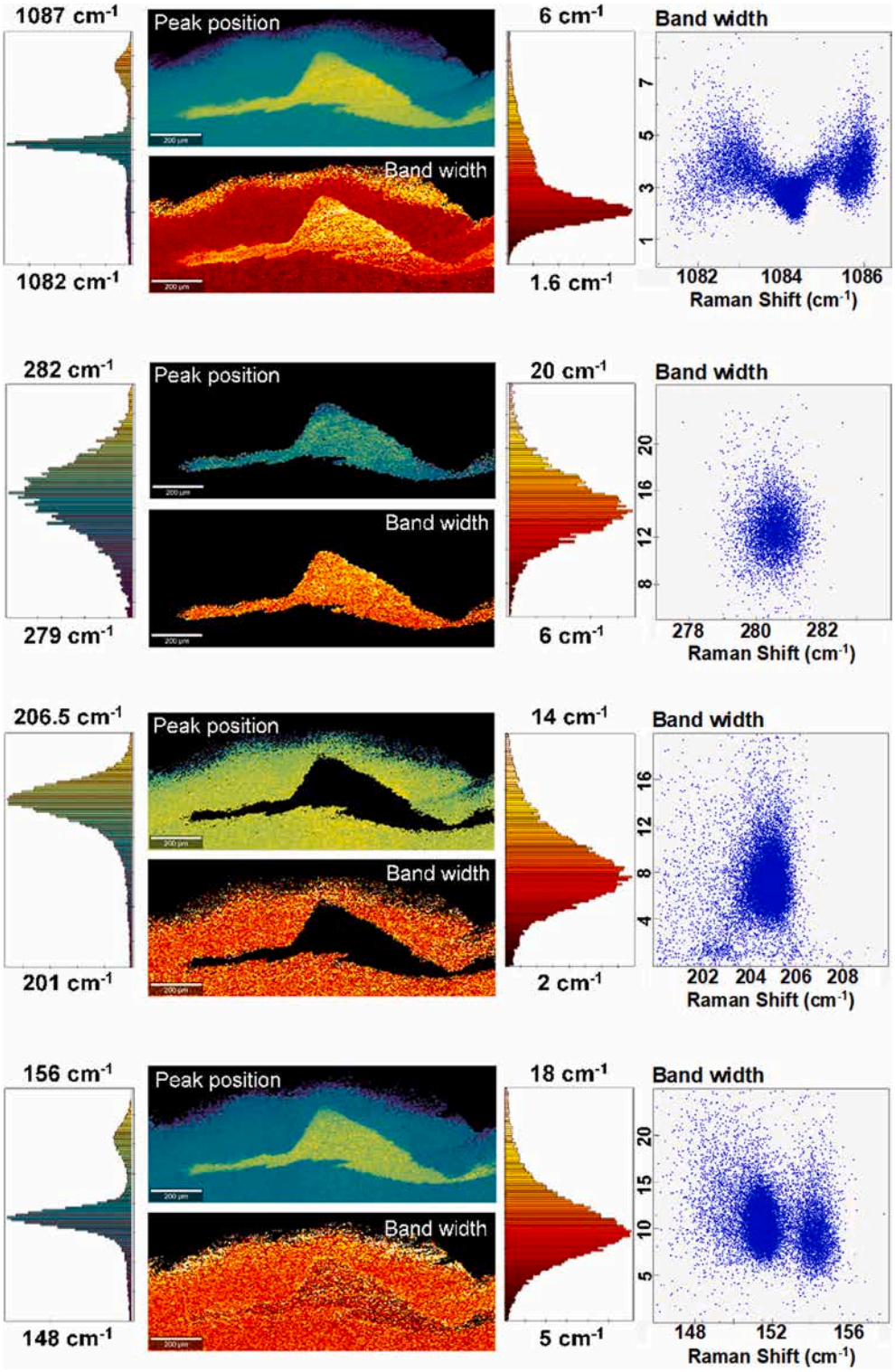

Fig. 5. Color-coded Raman mappings based on both peaks position and bands width of Lorentzian curves in four spectral regions centred around 150, 200, 280 and 1085 cm^{-1}. 52,500 spectra, scan area: 1360 × 538 μm^2, step size of around 3.6 μm. The histograms of shift distribution are shown for the position and width in two different color scales to make the results easier to read. The correlation map between Raman position and width shifts are shown on the right. White scale bar 200 μm.

confirm the presence of two minerals phases: aragonite and calcite. In Fig. 3C, three prominent IR absorption bands can be observed in the regions 1300–1600, 800–900 and 650–750 cm^{-1} (Table 1).

The characteristic peak positions of calcite (Farmer, 1974; Jones and Jackson, 1993) are observed between 1370 and 1390, at 870 and 711 cm^{-1}; these bands are commonly attributed to the asymmetric stretching modes and the asymmetric and symmetric deformations of the carbonate group, respectively (White, 1974). The absorption band at 711 cm^{-1} is doubly degenerated for the undistorted CO_3 groups. Consequently, as the carbonate groups become distorted, this mode splits into two components, revealing therefore the presence of aragonite phase. The other characteristic vibrational modes for aragonite are the out of plane bending mode ($\overline{\nu}_2$) at 854 cm^{-1} and the asymmetric stretching ($\overline{\nu}_3$) mode at 1432 cm^{-1}. The symmetric stretching ($\overline{\nu}_1$) mode

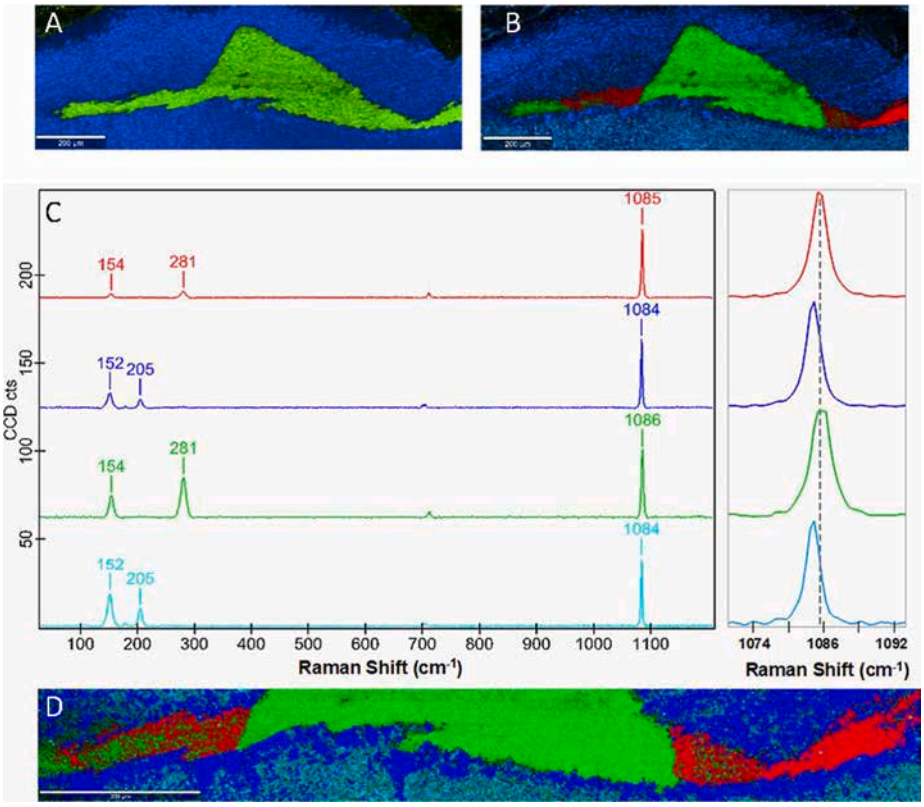

Fig. 6. Raman mapping based on 52,500 spectra recoded in 1360 × 538 μm^2 area. A) True component analysis identified 2 major spectral components. The identified components are shown in Figure C): the blue spectrum is characteristic of spherulitic aragonite and the green spectrum of calcite. B) True component analysis identified 4 major spectral components. The identified components are shown in Figure C): the blue spectrum is characteristic of spherulitic aragonite, the cyan spectrum of the nacreous layer and the green and red spectra of calcite. D) High-resolution Raman mapping based on 38,500 spectra recoded in 1100 × 140 μm^2 area. True component analysis confirmed 4 major spectral components. The identified components are similar to those determined in B: spherulitic aragonite (blue), nacreous layer (magenta) and calcite (green and red) phases. White scale bar 200 μm.

IR-inactive for the isolated carbonate ion. However, for aragonite, a very weak band are observed at 1082 cm^{-1} in the IR reflectivity spectrum as a result of the site-induced breakdown of the isolated anion selection rules. Let us note that for both aragonite and calcite, the asymmetric stretching mode, $\bar{\nu}_3$, are broad and asymmetric suggesting the carbonate groups are slightly distorted in each mineral phase (Dupuis et al., 1984; Zou et al., 2019).

It is interesting to note that the Raman spectra do not show any vibrational band beyond 1100 cm^{-1} as reported in our previous works (Hedegaard et al., 2006; Trinkler et al., 2011) when polyenes are observed. On the other hand, the modification of the baseline can always be associated to the presence of organic materials, a lack of good crystallinity or the presence of trace elements like Mn^{2+}, Mg^{2+} or Fe^{3+} replacing Ca^{2+} in carbonate (Rousseau et al., 2005; Trinkler et al., 2010). The color-coded Raman mapping based on the baseline intensity around 1100 cm^{-1} give a clear indication of the presence of more pronounced luminescence in both the nacreous layers and the periostracum (Fig. S1). In the following, the Raman spectra will be baseline-corrected before studying the spatial distribution of the $CaCO_3$ polymorphs and calcite-aragonite interfaces.

In order to get a better idea of the localization of both calcite and aragonite, FTIR mapping has been performed as well as a chemometric exploration of the hyperspectral dataset (Fig. 4). Principal component analysis (PCA) has been used to distinguish main features explaining the most variance in the dataset by finding a set of linearly independent variables. In Fig. 4.A2, the loading vector plot of the first component (PC1, 35% of the total variance) provides useful structural information in the wavenumber range 900–680 cm^{-1}, especially on the negatively correlated bands. The positive values are assigned to the position of vibrational bands of calcite and the negative ones to aragonite. The PC1 score image illustrated in Fig. 4A1 allows to reveal the spatial distribution of the two polymorphs; the blue region indicates the presence of aragonite, the pink-red region the presence of calcite. This figure shows an irregular area of calcite surrounded by aragonite. In order to better understand the transition between these two polymorphs a transect analysis was performed (Fig. 4B1). The spectra entitled Sp1 to Sp7 (Fig. 4B2) correspond to the position 1 to 7 in Fig. 4B1. The main features of spectra confirm the presence of pure aragonite (Sp1 and Sp7) and calcite (Sp4) phases. Between Sp2 and Sp6, a binary mixture of the calcium carbonate phases coexists, with a predominance of aragonite in Sp6 and calcite in Sp3 and Sp5 spectra.

However, by comparing the SP1 and SP7 spectra, it can be noted that the relative intensity of the bands at 853 and 690–720 cm^{-1} differs depending on whether a spherulitic or a nacreous layer is investigated. Indeed, the peak intensity ratio of the 853/700 cm^{-1} bands is greater than 3 in the case of spherulitic aragonite layer and of the order of 2 for a prismatic aragonite layer. The ratios are 2 and 1.5 respectively if we compare instead the intensities of the bands at 853 and 711 cm^{-1}. This difference is likely due to different crystallographic orientation and organisation. The spatial resolution used in FTIR was 20 μm, which made it difficult to study the calcite-nacreous layer interface at the micrometric scale. For this reason, confocal micro-Raman analyses were performed on the same area with higher spatial resolution.

In typical $CaCO_3$ Raman spectra, the more intense and narrow width band (Fig. 3) is the symmetric stretching mode $\bar{\nu}_1$ of the carbonate group (CO_3), which appears at 1085 for aragonite and 1086 cm^{-1} for calcite (Table 1). (Carteret et al., 2009) It is admitted that aragonite can be identified by the presence of two well-defined bands at 152 and 206 cm^{-1} attributed respectively to the translation and vibrational modes when calcite is characterized by two bands at 155 and 282 cm^{-1}.

Large area confocal Raman mapping was then performed on the same sample with a XY spatial resolution of approximately 3.6 μm in order to investigate the spatial distribution of the $CaCO_3$ polymorphs and calcite-aragonite interfaces. Peak and width shift analysis was performed in the vicinity of 4 spectral regions: 150, 200, 280 and 1085 cm^{-1}. For this purpose, the advanced fitting option in the WITec Project Plus software was used and a Lorentzian curve was fitted to the spectra (for each position of the map). The accurate position and full width at

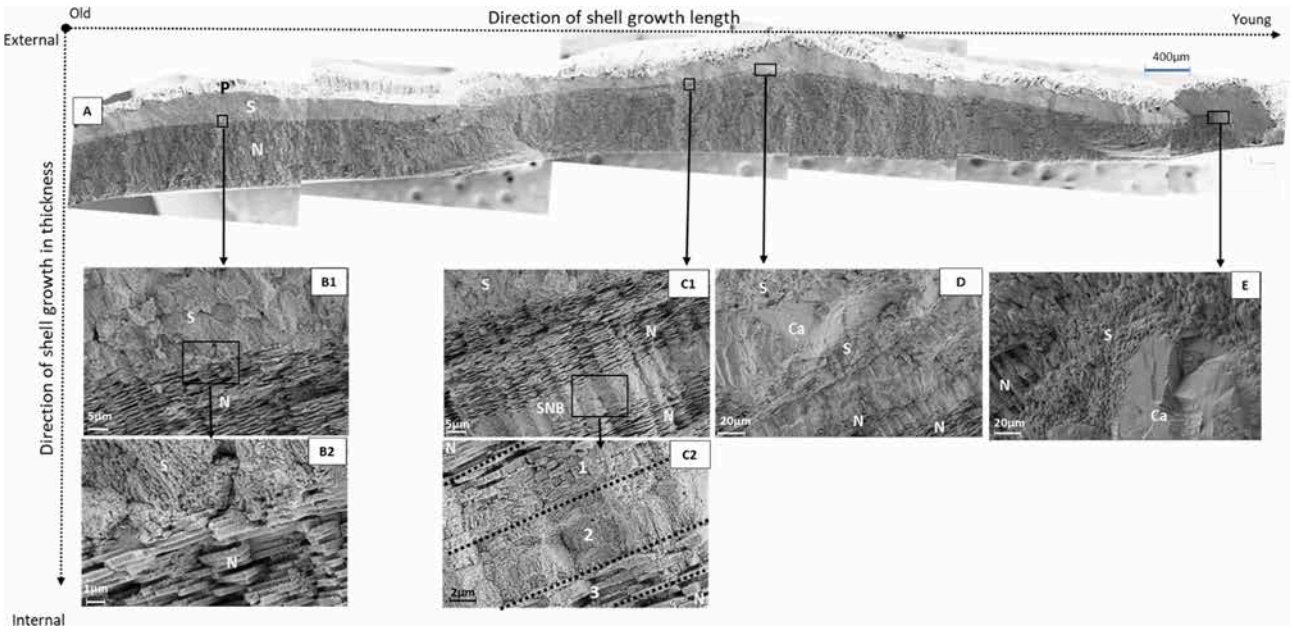

Fig. 7. Cross-section SEM image of abalone shell fracture showing the organization and microstructural diversity of the spherulitic layer (S), nacreous layer (N) and two areas of calcite (Ca). (A) The growth direction, in thickness, is from the top (periostracum, P) down nacreous inner layer (N) through the outer spherulitic layer (S). The growth direction in length is illustrated from the left to the right. The notation (B, C, D, E) corresponds to zooms in zones of the microstructures. Different mineral phases are reported: aragonitic layers (S for spherulitic and N for nacreous) and calcitic areas (Ca). Spherulitic / nacreous band (SNB) in the (C1) is a band in the nacreous layer.

half maximum (FWHM) of the Raman peaks were extracted for each selected spectral region to generate informative structural colormaps (Fig. 5). The histograms of shift distribution are systematically shown for the position and width in two different color scales. However, from these data, it is more easy to evaluate the variability of the results by plotting the correlation map between Raman position and width shifts.

In the 148–156 cm^{-1} range, 2 main density population (related to spectral features) are clearly observed (Fig. 5). According to Table 1, the lower Raman shift value is associated with aragonite (green zone) and the upper value with calcite (yellow zone). The correlation map shows that the mean value of the full width at half height (FWHM) of the calcite peak is slightly lower (red zone) than that associated with the aragonite peak (large orange area), but with a similar standard deviation (width of the distribution). So, from both graphical representations, it is possible to distinguish the shape of the calcite zone embedded in the aragonite.

If we look at the Raman images (Fig. 5) obtained from the peaks centred at 200 and 280 cm^{-1} it is very easy to locate the region attributed to aragonite and calcite. Contours can even be visualized in great detail because the distribution of peak and width shifts is close to a normal distribution, meaning the area color is rather uniform.

Finally, in the 1080–1088 cm^{-1} range, 2 main density population are clearly observed (Fig. 5). The lower wavenumber area (green area) is attributed to aragonite and the yellow one to calcite (similar to the map obtained from the 148–156 cm^{-1} range). It can be seen from the correlation map that the mean width of the peak associated with calcite is higher and more spread out than aragonite. Accordingly, all of these results demonstrated that confocal micro-Raman mapping is a powerful tool to reveal and identify the spatial distribution of carbonate polymorphs, even if the structural arrangements are complex.

In order to investigate the calcite-aragonite interface close to the nacreous layer, a specific Raman mapping was performed with 2D map step size of 2 µm. In Fig. S2, the results are essentially similar to those presented previously (Fig. 5), however, some differences can be more easily appreciated in the distribution of the positions of certain peaks and in particular over the spectral range 1000–1080 cm^{-1}. Indeed, the results show a bimodal distribution for the band located in the vicinity of 1087 cm^{-1}, attributed to the calcite zone. By paying more attention to the distribution of widths of this band, it can also be seen that the right and left parts of the calcite are characterized by a narrower width (dark red color). These spectral features, associated with slight color changes on the mapping can also be observed on the characteristic bands around 280 and 153 cm^{-1}; the darkening of the right part of the calcite is associated with narrower widths.

In order to go further in the analysis of Raman mapping, a True Component Analysis (TCA) was performed (Fig. 6). Basically, TCA identified spectral components that are most prevalent in the dataset. The average spectra, which can be extracted from the components, is then helpful to identify molecular structures and reveal changes in crystallinity, orientation or molecular conformation. With the first 2 components, the spectral signatures coded in blue (component 1) and in green (component 2) in Fig. 6A, are respectively the zones of aragonite and calcite (Fig. 6A), already discussed above. However, with TCA, 4 major spectral components can be identified (Fig. 6B-C). One of the additional components, coded in light blue, is typically characteristic of aragonite. Indeed, the position of the main peaks are similar to the first component with a strong band at 1084 cm^{-1} and two well-defined bands at 152 and 205 cm^{-1}. However, changes were observed in the relative intensity of the latter peaks and the symmetric stretching mode $\bar{\nu}_1$ of the carbonate group. So, the result which is certainly the most important of this analysis is that the confocal Raman mapping and the TCA were able to successfully discriminate the well-ordered columnar organization of the inner nacreous layer from the spherulitic aragonite layer. Consequently, in Fig. 6D, it clearly appears that the calcitic zone is surrounded by a spherulitic structure and a complex and irregular interface with the inner nacreous layer. Similar results were found for a selection of wild and farmed samples, confirming that the calcitic zone is systematically separated from the nacreous zone by a thin layer of spherulitic aragonite. The fourth component, whose Raman spectrum is shown in red in Fig. 6C, is characteristic of a calcitic structure. Compared to the major calcitic area (colored in green), changes were observed with this component. Indeed, the relative intensity of low wavenumber peaks and the intense peak at 1085 cm^{-1} are different and the full width at half maximum of the symmetric stretching mode $\bar{\nu}_1$ of the carbonate group is slightly reduced. This result confirms what we previously described in

Fig. 5, meaning that this calcitic zone (coded in red in Fig. 6D) is probably associated with a better ordered structure that the coded green area (spectrum characterized by a broader $\bar{\nu}_1$ mode).

The position of symmetric CO_3 stretching mode, located at 1085 cm^{-1}, is known to shift (and increase for the respective width) with additional cations substitution (e.g. Mg^{2+}, Mn^{2+}, Fe^{2+}) (Bischoff et al., 1985, Edwards et al., 2005). The position of this band cannot been used to determine the type of the cation since its frequency depends only on the movement of the O atoms (Rutt and Nicola, 1974).

So, in order to locate calcite areas and la nature des cations, we decided to investigate by EDS the chemical composition of the shell and look for the incorporation of trace elements in the lattice of calcite-type carbonates (Veizer, 1983). The EDS maps (Fig. S3) revealed chemical zonation between calcite in the center and aragonite around it. The results clearly show a Mg enrichment (Fig. S3 B-D) coupled with a Na (Fig. S3 C-D) depletion for calcite in contrast to aragonite. The cations smaller than Ca can easily substitute Ca in the rhombohedral cell of calcite whereas the large orthorhombic cell of aragonite can incorporate elements with bigger ionic radius (such as Na).

Calcite contains a very low percentage of Mg with a Mg/Ca ratio < 1% estimated by EDS with both standardless ZAF and phiRo(z) methods regarding net intensities, weight percent (wt%) and normalized wt% (Tab.2 S4). This could explain both the small broadening of the 1085 cm^{-1} band observed by Raman, and the absence of displacement of the IR-active bending mode from 711 cm^{-1} to 719 cm^{-1} characteristic of magnesian calcite (Gayathri et al., 2007).

3.2. Shell organization and microstructure

SEM observations shown in Fig. 7A illustrate a full cross-section of a shell (10.5 mm long) at different length scales. The most recently formed inner shell surface is on the right of the image and the oldest on the left. The cross-section can be divided into three distinct layers: the external surface consists of the periostracum (P) and two distinct aragonitic layers, previously identified as the outer spherulitic (S) and the inner nacreous layer (N). SEM investigations allowed to characterize the shell microstructure and biomineral organization. The outer layer (S) varies from 180 to 300 μm and the inner layer (N) between 300 and 700 μm.

Magnification shown in Fig. 7B1-B2 revealed the structure of the spherulitic outer layer and the typical well-ordered columnar organization of the inner nacreous layer with nacre platelets of about 0.2 to 0.4 μm thick. The abrupt transition from the spherulitic layer (S) to the nacre (N) was already reported on the abalone shell (Lin and Meyers, 2005).

In Fig. 7C1, a large compact band named here spherulitic / nacreous band (SNB), about 14.5 μm thick, can be observed between two nacreous layers. At higher magnification (Fig. 7C2), this band can be separated into three domains in the direction of shell thickness growth from top (older) to bottom (younger). Layer 2 (6 μm thick), which represents the central zone, is mainly characterized by a dense and compact spherulitic microstructure. The regions 1 and 3, are mainly interfacial layers approximately 6 μm thick between the central spherulitic layer and the surrounding prismatic aragonite layers. These unusual prismatic-spherulitic-prismatic aragonite interfaces observed on the different shells, could correspond to the specific dense layer crossing the nacreous layer observed by Philippon (1974). So far, no study has focused on understanding why such spherulitic bands appear in nacreous layer during growth. Environmental factors (water composition, temperature, pH, salinity, etc.) or changes in physiological status and in metabolic activity (reproduction, stress response, etc.) may be reasonably invoked.

Compared to zones B and C which both contain only aragonite (spherulitic and nacreous layers), the zones D and E sections revealed (Fig. 7D, E) prismatic microstructures; dimensions vary between 20 and 150 μm wide. These microstructures correspond respectively to the calcite (Ca) areas previously detected and characterized by vibrational microscopy analysis. Our SEM observations confirm therefore that the calcitic biominerals are surrounded by spherulitic microstructures (Fig. 7D, E). More surprisingly, we also noticed in Fig. 7D the presence of a 10 μm nacreous layer (N) incorporated between two spherulitic regions. This particular structural arrangement demonstrates once again the complexity of growth during this period and the difficulty of stabilizing a structural phase.

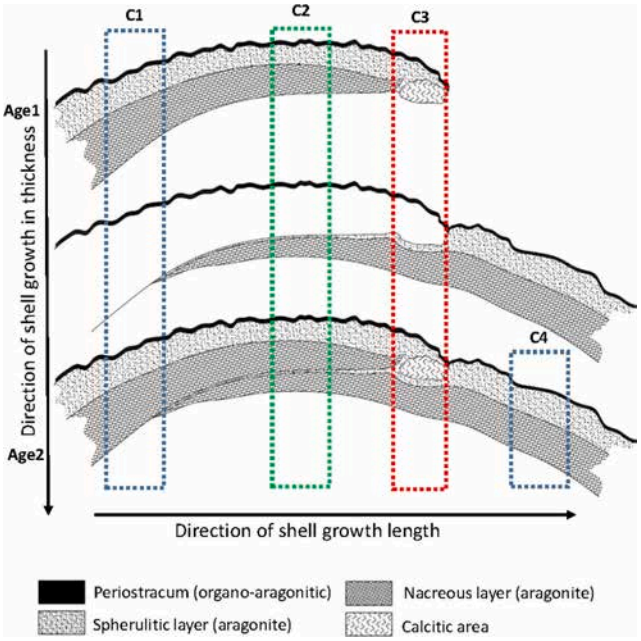

Fig. 8. Schematic reconstruction of mineral layers and microstructures in relative chronology throughout the growth ages (Age1 and Age2) in the adulthood shell of abalone Haliotis tuberculata. This model shows the variations of the mineralogical phases and their microstructural morphology according to the position of the sections (C1, C2, C3, C4). The direction of growth is from top (Age1) to bottom (Age2) and from left to right.

Observing the cross-section of abalone shell by SEM helped us to better understand the hierarchical organization of these non-classical structures compared to the two aragonite layers (S and N) structures. We therefore proposed, in Fig. 8, a simplified reconstruction of the different layers and microstructures in relative chronology throughout the growth ages (between age 1 and age 2) in adulthood shell of *H. tuberculata*.

In the various cuts (C1 to C4) we are able to describe the different stages of apparition of the microstructures and the biominerals. Actually, in sections C1 and C4 we only observe the presence of the two classical layers (S and N) confirming the conclusions of Stolkowski (1951) who did not see any calcite in the outer layer. In section C2, a spherulitic and a nacreous layers are present in age 1, but if we look at the "Age2" a small compact spherulitic layer can be observed within the nacreous layer. Such a result could then explain the interpretation of Philippon (1974) who reports a nacreous layer crossed by compact bands. Finally, in section C3, in particular at the "Age2", 4 layers should be observed, which confirms the three layers reported by Bøggild (1930) and Dauphin et al. (2014). Finally, if we look at the diagram of the section "Age2" we notice the presence of calcite, in the form of small spot, confirming the observations of both Bøggild (1930), Bouillon (1958), Dauphin et al. (2014), Mutvei et al. (1985) and Sabatier (1953). So, our schematic reconstruction of mineral layers and microstructures in relative chronology throughout the growth ages (Fig. 8) can explain, for the first time, the reasons for past controversies. Indeed, probably due to individual variations within the abalone (age, season, genetic origin) and/or differences in spatial resolution and/or orientation of the cut, observations can vary considerably and lead to very different conclusions.

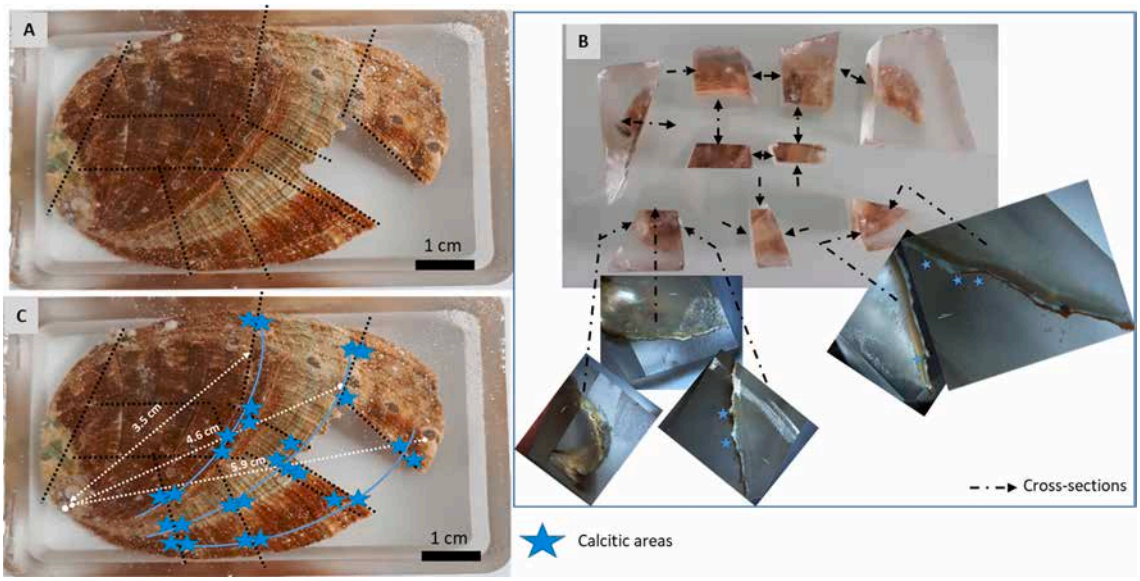

Fig. 9. Location of cuts in abalone Haliotis tuberculata shell adult (6 cm). A) Location of the sections. B) The nine pieces of the shell and the sections that are observed and photographed under binocular. C) The calcite zones were marked with stars and then connected to each other by continuous lines. The white arrows indicate the direction of growth and the lengths at which the calcitic streaks are found.

So, we demonstrate here the need to establish a common methodology to study the section plans or to carefully specify the location and orientation of the cross-section. These factors are key elements in comparing the results of the different analyses, observations and interpretations between authors.

In order to better understand where these calcitic areas can be found in the shell, we embedded five shells in resin before cutting them into nine pieces along different axes (Fig. 9).

Each piece was studied meticulously under a binocular then the optically identified areas were analyzed by Raman under microscope to verify the presence of calcitic areas within the aragonite shell. Let us point out that the size and shapes of the calcitic zone varies with the orientation of the cross-section. After having marked the position of the calcite areas (illustrated by stars in Fig. 9B and 9C), we realized that their positions are not distributed randomly. Indeed, if we connect these marks by a line their spatial locations are occur along growth increments (Fig. 9C). Our observations reveal that the five shells of *H. tuberculata* contain the same number of streaks (lines perpendicular to the directions of shell length growth) suggesting that they probably are of the same age.

To our knowledge it is the first time that the spatial repartition of calcitic zones are reported for abalone shell. This result therefore opens up new fields of investigation. Current projects are now aiming to study shells of different ages and at different period of the year in order to study whether these streaks correspond more to a stage of gonadal development and / or a specific response to environmental changes.

4. Conclusions

The shell of *Haliotis tuberculata* mainly consists of two aragonite layers, a nacreous inner layer and a spherulitic outer layer. Our studies carried out by FTIR and classical Raman, on a large selection of wild and farmed adult European abalone *H. tuberculata*, confirm in 100% of cases (30 shells) the systematic presence, in the spherulitic layer, of irregular calcitic zones of varying sizes. By using for the first-time high resolution confocal micro-Raman mapping we have then clearly shown, that the calcitic zone is separated from the nacreous zone by a thin layer of spherulitic aragonite, thus clarifying the complex spatial distribution of the different mineral phases at microscale. SEM observations revealed that the inner nacreous layer can also contain spherulitic microstructures, suggesting the importance of spherulitic structures in biomineralization and in particular for shell continuity or regrowth. Finally, a schematic reconstruction of different layers and microstructures in relative chronology throughout the growth ages allowed us to better understand the reasons of the controversial observations reported in previous published papers for more than 70 years. We clearly explained why the location of the calcitic zones depends on the position of the section plan and why the dimension of the calcitic zone varies with the orientation of the cross-section.

Finally, through the analysis of puzzle sections of shells we demonstrated for the first time that these calcitic areas formed streaks perpendicular to the directions of length growth. Given the importance of this observation, our future work will therefore aim to study the influence of different environmental parameters (temperature, pH, food, etc.) on the appearance and localization of these calcitic zones. If the results are relevant we might clarify the relative sensitivity of abalone to climate changes.

CRediT authorship contribution statement

Aïcha Badou: Conceptualization, Methodology, Formal analysis, Investigation, Writing – original draft, Writing – review & editing, Supervision. **Sylvain Pont:** Investigation, Visualization. **Stéphanie Auzoux-Bordenave:** Investigation, Funding acquisition. **Morgane Lebreton:** Methodology, Investigation. **Jean-François Bardeau:** Conceptualization, Methodology, Formal analysis, Investigation, Writing – original draft, Writing – review & editing.

Declaration of Competing Interest

The authors declare that they have no known competing financial interests or personal relationships that could have appeared to influence the work reported in this paper.

Acknowledgements

The specimen collections and shell preparations were carried out within the framework of the ATM program “Biomineralization” of the MNHN funded by the Ministère délégué à l’Enseignement Supérieur et à la Recherche (Paris, France). We thank Sylvain Huchette from the

France Haliotis farm (Plouguerneau, France) who provided abalone shells for the experiments.

Appendix A. Supplementary material

Supplementary data to this article can be found online at https://doi.org/10.1016/j.jsb.2022.107854.

References

Addadi, L., Joester, D., Nudelman, F., Weiner, S., 2006. Mollusk shell formation: a source of new concepts for understanding biomineralization processes. Chem. Eur. J. 12 (4), 980–987.

Ajili, W., Laurent, G., Menguy, N., Gansmuller, A., Huchette S., Auzoux-Bordenave, S., Nassif, N., Azais, T., 2020. Chemical heterogeneities within the disordered mineral domains of aragonite platelets in nacre from the European abalone *Haliotis tuberculate*. J. Phys. Chem. C124, 26, 14118–14130. doi: https://doi.org/10.1021/acs.jpcc.0c00280.

Amarie, S., Zaslansky, P., Kajihira, Y., Griesshaber, E., Schmahl, W.W., Keilmann, F., 2012. Nano-FTIR chemical mapping of minerals in biological materials. Beilstein J. Nanotechol. 3, 312–323.

Auzoux-Bordenave, S., Brahmi, C., Badou, A., de Rafélis, M., Huchette, S., 2015. Shell growth, microstructure and composition over the development cycle of the European abalone *Haliotis tuberculata*. Mar. Biol 162, 687–697. https://doi.org/10.1007/s00227-015-2615-y.

Auzoux-Bordenave, S., Badou, A., Gaume, B., Berland, S., Helléouet, M.-N., Milet, C., Huchette, S., 2010. Ultrastructure, chemistry and mineralogy of the growing shell of the European abalone *Haliotis tuberculata*. J. Struct. Biol. 171 (3), 277–290.

Beuvier, T., Bardeau, J.-F., Calvignac, B., Corbel, G., Hindré, F., Grenèche, J.-M., Boury, F., Gibaud, A., 2013. Phase transformations in $CaCO_3$/iron oxide composite induced by thermal treatment and laser irradiation. J. Raman Spectrosc. 44, 489–495. https://doi.org/10.1002/jrs.4200.

Bischoff, W.D., Sharma, S.K., Mackenzie, F.T., 1985. Carbonate ion disorder in synthetic and biogenic magnesian calcites: A Raman spectral study. Am. Min. 70, 581–589. https://pubs.geoscienceworld.org/msa/ammin/article-abstract/70/5-6/581/41751/Carbonate-ion-disorder-in-synthetic-and-biogenic.

Blank, S., Arnoldi, M., Khoshnavaz, S., Treccani, L., Kuntz, M., Mann, K., Grathwohl, G., Fritz, M., 2003. The nacre protein perlucin nucleates growth of calcium carbonate crystals. J. Microsc. 212, 280–291. https://onlinelibrary.wiley.com/doi/10.1111/j.1365-2818.2003.01263.x.

Bøggild, O.B., 1930. The shell structure of the Molluscs. Kongelige Danske Videnskabernes Selskabs Skrifter, 9. Kjobenhavn, pp. 233–326.

Bouillon, J., 1958. Quelques observations sur la nature de la coquille chez les mollusques. Société Royale zoologique de Belgique, Annales LXXXIX 1958–9, 231–237.

Brown, C.H., 1975. Structural materials in animals. Pitman eds. (London), 448 p.

Carteret, C., Dandeu, A., Moussaoui, S., Muhr, H., Humbert, B., Plasari, E., 2009. Polymorphism studied by lattice phonon Raman spectroscopy and statistical mixture analysis method. Application to calcium carbonate polymorphs during batch crystallization. Cryst. Growth Des. 9 (2), 807–812.

Carteret, C., De la Pierre, M., Dossot, M., Pascale, F., Erba, A., Dovesi, R., 2013. The vibrational spectrum of $CaCO_3$ aragonite: A combined experimental and quantum-mechanical investigation. J. Chem. Phys. 138, 014201–14212. https://doi.org/10.1063/1.4772960.

Copper, S.N., Gilbert, P., Metzler, R.A., 2009. Theoretical characterization of a model of aragonite crystal orientation in red abalone nacre. J. Phys. A: Math. Theor. 42 (12), 125101.

Courtois de Viçose, G., Viera, M.P., Bilbao, A., Izquierdo, M.S., 2007. Embryonic and larval development of *Haliotis tuberculata coccinea* Reeve: an indexed microphotographic sequence. J. Shellfish Res. 26, 847–854. https://doi.org/10.2983/0730-8000(2007)26[847:EALDOH]2.0.CO;2.

Couture, L., 1947. Vibrational spectra of single ionic crystals. Ann. Phys. 2, 5–94.

Cusack, M., Guo, D., Chung, P., Kamenos, N.A., 2013. Biomineral repair of abalone shell apertures. J. Struct. Biol. 183, 165–171. https://doi.org/10.1016/j.jsb.2013.05.010.

Dandeu, A., Humbert, B., Carteret, C., Muhr, H., Plasari, E., Bossoutrot, J.-M., 2006. Raman spectroscopy—A powerful tool for the quantitative determination of the composition of polymorph mixtures: Application to $CaCO_3$ polymorph mixtures". Chem. Eng. Technol. 29, 221–225. https://doi.org/10.1002/ceat.200500354.

Dauphin, Y., Cuif, J.-P., Mutvei, H., Denis, A., 1989. Mineralogy, chemistry and ultrastructure of the external shell-layer in ten species of Haliotis with reference to *Haliotis tuberculata* (Mollusca: Archaeogastropoda). Bull. Geol. Inst. Univ. Uppsala, NS 15, 7–38.

Dauphin, Y., Cuif, J.P., Castillo-Michel, H., Chevallard, C., Farre, B., Meiborn, A., 2014. Unusual micrometric calcite–aragonite interface in the abalone shell Haliotis (mollusca, gastropoda). Microsc. Microanal. 20, 274–276. https://doi.org/10.1017/S1431927613013718.

De La Pierre, M., Carteret, C., Maschio, L., André, E., Orlando, R., Dovesi, R., 2014. The Raman spectrum of $CaCO_3$ polymorphs calcite and aragonite: A combined experimental and computational study. J. Chem. Phys. 140 (16), 164509.

De Leeuw, N.H., Parker, S.C., 1998. Surface structure and morphology of calcium carbonate polymorphs calcite, aragonite, and vaterite: An atomistic approach. J. Phys. Chem. B 102, 2914–2922. https://doi.org/10.1021/jp973210f.

Drouin, D., Couture, A.R., Joly, D., Tastet, X., Aimez, V., Gauvin, R., 2007. CASINO V2.42: a fast and easy-to-use modeling tool for scanning electron microscopy and microanalysis users. Scanning 29 (3), 92–101. https://doi.org/10.1002/sca.20000.

Dupuis, T., Ducloux, J., Butel, P., Nahon, D., 1984. Etude par spectrographie infrarouge d'un encroutement calcaire sous galet. Mise en évidence et modélisation expérimentale d'une suite minérale évolutive à partir de carbonate de calcium amorphe. Clay Miner. 19, 605–614. https://doi.org/10.1180/claymin.1984.019.4.07.

Edwards, H.G.M., Villar, S.E.J., Jehlicka, J., Munshi, T., 2005. FT-Raman spectroscopic study of calcium-rich and magnesium-rich carbonate minerals. Spectrochim. Acta, Part A61, 2273–2280. https://doi.org/10.1016/j.saa.2005.02.026.

Falini, G., Albeck, S., Weiner, S., Addadi, L., 1996. Control of aragonite or calcite polymorphism by mollusk shell macromolecules. Science 271, 67–69. https://doi.org/10.1126/science.271.5245.67.

Farmer, V.C., 1974. The Infrared Spectra of Minerals. London (Mineralogical Society), x + 539 pp., 219 figs.

Frech, R., Wang, E.C., Bates, J.B., 1980. The IR and Raman spectra of $CaCO_3$ (aragonite). Spectrochim Acta 36A, 915–919. https://doi.org/10.1016/0584-8539(80)80044-4.

Frenzel, M., Harper, E.M., 2011. Micro-structure and chemical composition of vateritic deformities occurring in the bivalve *Corbicula fluminea* (Müller, 1774). J. Struct. Biol. 174, 321–332. https://doi.org/10.1016/j.jsb.2011.02.002.

Gaume, B., Fouchereau-Peron, M., Badou, A., Helléouet, M.-N., Huchette, S., Auzoux-Bordenave, S., 2011. Biomineralization markers during early shell formation in the European abalone *Haliotis tuberculata*. Linnaeus. Mar. Biol. 158, 341–353. https://doi.org/10.1007/s00227-010-1562-x.

Gayathri, S., Lakshminarayanan, R., Morse, D.E., Kini, R.M., Valiyaveettil, S., 2007. In vitro study of magnesium-calcite biomineralization in the skeletal materials of the seastar Pisaster giganteus. Chem. Eur. J. 13, 3262–3268. https://doi.org/10.1002/chem.200600825.

Gilbert, P.U.P.A., Metzler, R.A., Zhou, D., Scholl, A., Doran, A., Young, A., Kunz, M., Tamura, N., Coppersmith, S.N., 2008. Gradual ordering in red abalone nacre. J. Am. Chem. Soc. 130 (51), 17519–17527. https://pubs.acs.org/doi/10.1021/ja8065495.

Gries, K., Kröger, R., Kübel, C., Schowalter, M., Fritz, M., Rosenauer, A., 2009. Correlation of the orientation of stacked aragonite platelets in nacre and their connection via mineral bridges. Ultramicroscopy 109 (3), 230–236. https://pubmed.ncbi.nlm.nih.gov/19117678/.

Hedegaard, C., Bardeau, J.-F., Chateigner, D., 2006. Molluscan shell pigments: an in situ resonance Raman study. J. Molluscan Stud. 72, 157–162. https://doi.org/10.1093/mollus/eyi062.

Heinemann, F., Launspach, M., Gries, K., Fritz, M., 2011. Gastropod nacre: Structure, properties and growth — Biological, chemical and physical basics. Biophys. Chem. 153, 126–153. https://doi.org/10.1016/j.bpc.2010.11.003.

Hickman, C.S., 2001. Evolution and development of gastropod larval shell morphology: experimental evidence for mechanical defense and repair. Evol. Dev. 3, 18–23. https://doi.org/10.1046/j.1525-142x.2001.01003.x.

Iwata, K., 1980. Mineralization and architecture of the larval shell of *Haliotis discus hannai* Ino (Archaeogastropoda). J. Fac. Sci. Hokkaido Univ. Ser. 4 (19), 305–320.

Jackson, D.J., McDougall, C., Woodcroft, B., Moase, P., Rose, R.A., Kube, M., Reinhardt, R., Rokhsar, D.S., Montagnani, C., Joubert, C., Piquemal, D., Degnan, B. M., 2010. Parallel evolution of nacre building gene sets in molluscs. Mol. Biol. Evol. 27 (3), 591–608. https://doi.org/10.1093/molbev/msp278. https://academic.oup.com/mbe/article/27/3/591/1000371.

Jardillier, E., Rousseau, M., Gendron-Badou, A., Fröhlich, F., Smith, D., Martin, M., Helléouet, M.N., Huchette, S., Doumenc, D., Auzoux-Bordenave, S., 2008. A morphological and structural study of the larval shell from the abalone *Haliotis tuberculata*. Mar. Biol. 154, 735–744. https://doi.org/10.1007/s00227-008-0966-3.

Jolivet, A., Chauvaud, L., Huchette, S., Legoff, C., Thébault, J., Nasreddine, K., Bernd R. Schöne, B.R., Clavier, J., 2015. The ormer (Haliotis tuberculata): A new, promising paleoclimatic tool. Palaeogeogr., Palaeoclimatol., Palaeoecol. 427, 32–40. https://doi.org/10.1016/j.palaeo.2015.03.032.

Jolly, C., Berland, S., Milet, C., Borzeix, S., Lopez, E., Doumenc, D., 2004. Zonal localization of shell matrix proteins in mantle of *Haliotis tuberculata* (Mollusca, Gastropoda). Mar. Biotechnol. 6, 541–551. https://doi.org/10.1007/s10126-004-3129-7.

Jones, G.C., Jackson, B., 1993. Infrared Transmission Spectra of Carbonate Minerals. Chapman et Hall, London, Glasgow, New York, Tokyo, Melbourne, Madras. DOI: https://doi.org/10.1017/S0016756800011894.

Kaczorowska, B., Hacura, A., Kupka, T., Wrzalik, R., Talik, E., Pasterny, G., Matuszewska, A., 2003. Spectroscopic characterization of natural corals. Anal. Bioanal. Chem. 377 (6), 1032–1037. https://pubmed.ncbi.nlm.nih.gov/12955275/.

Kessel, E., 1935. Über den bau der Haliotis-Schale. Zool Anzeiger. 112, 290–329.

Levi-Kalisman, Y., Falini, G., Addadi, L., Weiner, S., 2001. Structure of the nacreous organic matrix of a bivalve mollusk shell examined in the hydrated state using cryo-TEM. J. Struct. Biol. 135, 8–17. https://doi.org/10.1006/jsbi.2001.4372.

Lifshin, E., Gauvin, R., 2003. Precision and detection limits for EDS analysis in the SEM. Micros. Today 11 (5), 46–49. https://doi.org/10.1017/S1551929500053256.

Lin, A., Meyers, M.A., 2005. Growth and structure in abalone shell. Mater. Sci. Eng. A 390, 27–41. https://doi.org/10.1016/j.msea.2004.06.072.

Lopez, M.I., Chen, P.Y., McKittrick, J., Meyers, M.A., 2011. Growth of nacre in abalone: Seasonal and feeding effects. Mater. Sci. Eng. C 31, 238–245. https://doi.org/10.1016/j.msec.2010.09.003.

Marin, F., Luquet, G., Marie, B., Medakovic, D., 2008. Molluscan shell proteins: Primary structure, origin, and evolution. Curr. Top. Dev. Biol. 80, 209–276. https://doi.org/10.1016/S0070-2153(07)80006-8.

Mutvei, H., Dauphin, Y., Cuif, J.P., 1985. Observations sur l'organisation de la couche externe du test des Haliotis ~Gastropoda!: Un cas exceptionnel de variabilité

minéralogique et microstructurale. Bull. Mus. Natl. Hist. Nat. Paris, 4è sér, 7A1, 73–91.
Newbury, D., Ritchie, N., Mengason, M., Scott, K., 2017. SEM/EDS Trace Analysis: Limits Imposed by Fluorescence of the Detector. Microsc. Microanal. 23 (S1), 1026–1027. https://doi.org/10.1017/S1431927617005797.
Philippon, J., 1974. Structure et composition minéralogique de la coquille de Gastropodes actuels et fossiles. CERPAB, notes et contributions, n° 7: 88.
Pokroy, B., Fieramosca, J.S., Von Dreele, R.B., Fitch, A.N., Caspi, E.N., Zolotoyabko, E., 2007. Atomic structure of biogenic aragonite. Chem. Mater. 19, 3244–3251. https://doi.org/10.1021/cm070187u.
Rousseau, M., Lopez, E., Couté, A., Mascarel, G., Smith, D.C., Naslain, R., Bourrat, X., 2005. Sheet nacre growth mechanism: a Voronoi model. J. Struc. Biol. 149, 149–157. https://doi.org/10.1016/j.jsb.2004.09.005.
Rutt, H.N., Nicola, J.H., 1974. Raman spectra of carbonates of calcite structure. J. Physiol. C 7, 4522–4528. https://doi.org/10.1088/0022-3719/7/24/015.
Sabatier, G., 1953. Application de la diffraction des rayons X à l'étude des coquilles de Mollusques. Cahiers des Naturalistes N.S., 8.
Schneider, A.S., Heiland, B., Peter, N.J., Guth, C., Arzt, E., Weiss, I.M., 2012. Hierarchical super-structure identified by polarized light microscopy, electron microscopy and nanoindentation: Implications for the limits of biological control over the growth mode of abalone sea shells. BMC Biophys. 5 (1), 19–31. https://doi.org/10.1186/2046-1682-5-19.
Schrader, B., Schulz, H., Andreev, G.N., Klump, H.H., Sawatzki, J., 2000. Non-destructive NIR-FT-Raman spectroscopy of plant and animal tissues, of food and works of art. Talanta 53, 35–45. https://doi.org/10.1016/s0039-9140(00)00385-4.
Spann, N., Harper, E.M., Aldridge, D.C., 2010. The unusual mineral vaterite in shells of the freshwater bivalve *Corbicula fluminea* from the UK. Naturwissenschaften 97, 743–751. https://doi.org/10.1007/s00114-010-0692-9.
Stolkowski, J., 1951. Essai sur le déterminisme des formes minéralogiques du calcaire chez les êtres vivants. Annals Inst. Océanogr. 26, 1–113.
Trinkler, N., Bardeau, J.-F., Marin, F., Labonne, M., Jolivet, A., Crassous, P., Paillard, C., 2011. Mineral phase in shell repair of Manila clam *Venerupis philippinarum* affected by brown ring disease. Dis. Aquat. Organ. 93 (2), 149–162. https://doi.org/10.3354/dao02288.
Trinkler, N., Labonne, M., Marin, F., Jolivet, A., Bohn, M., Poulain, C., Bardeau, J.-F., Paillard, C., 2010. Clam shell repair from the brown ring disease: a study of the organic matrix using Confocal Raman micro-spectrometry and WDS microprobe. Anal. Bioanal. Chem. 396, 555–567. https://doi.org/10.1007/s00216-009-3114-0.
Urmos, J., Sharma, S.K., Mackenzie, F.T., 1991. Characterization of some biogenic carbonates with Raman spectroscopy. Am. Mineral. 76, 641–646.
Valenzano, L., Torres, F.J., Doll, K., Pascale, F., Zicovich-Wilson, C.M., Dovesi, R., 2006. Ab Initio study of the vibrational spectrum and related properties of crystalline compounds: The case of $CaCO_3$ calcite. Z. Phys. Chem. 220, 893–912. https://doi.org/10.1524/zpch.2006.220.7.893.
Veizer, J., 1983. Carbonates: mineralogy and chemistry. Reviews in Mineralogy Vol. 11, R. J. Reeder Editor, 265-300.
Watabe, N., 1988. Shell structure in the mollusca, vol. 11. Academic Press: New York, pp. 69–104.
White, W.B., 1974. The carbonate minerals. In: Farmer, V.C. (Ed.), The Infrared Spectra of Minerals. Mineralogical Society of London, pp. 227–284. https://doi.org/10.1180/mono-4.12.
Wilbur, K.M., Saleuddin, A.S.M., 1983. Shell formation. In: The Mollusca, vol. 4. Academic Press, New York, pp. 235–285. https://doi.org/10.1016/B978-0-12-751404-8.50014-1.
Yao, N., Epstein, A.K., Liu, W.W., Sauer, F., Yang, N., 2008. Organic–inorganic interfaces and spiral growth in nacre. J. R. Soc. Interface 6, 367–376.
Zakaria, F.Z., Mihály, J., Sajó, I., Katona, R., Hajba, L., Aziz, F.A., Mink, J., 2008. FT-Raman and FTIR spectroscopic characterization of biogenic carbonates from Philippine venus seashell and Porites sp. coral. J. Raman Spectrosc. 39, 1204–1209. https://doi.org/10.1002/jrs.1964.
Zou, Z., Habraken, W.J.E.M., Matveeva, G., Jensen, A.C.S., Bertinetti, L., Hood, M.A., Sun, C.-Y., Gilbert, P.U.P.A., Polishchuk, I., Pokroy, B., Mahamid, J., Politi, Y., Weiner, S., Werner, P., Bette, S., Dinnebier, R., Kolb, U., Zolotoyabko, E., Fratz, P., 2019. A hydrated crystalline calcium carbonate phase: Calcium carbonate hemihydrate. Science 363, 396–400. https://doi.org/10.1126/science.aav0210.